Spatiotemporally Modulated Gyrators with Extended Bandwidth through Dual-Sideband Operation

Saeed Keshavarz and Dimitrios L. Sounas*

Department of Electrical and Computer Engineering, Wayne State University, Detroit, Michigan 48202, USA

(Received 9 June 2022; accepted 29 September 2022; published 27 October 2022)

One of the major challenges in the design of nonreciprocal devices is the application of magnetic biasing. This problem has motivated a flurry of work for the development of magnetless nonreciprocal devices, with spatiotemporal modulation being one of the most promising approaches to this end. The most fundamental nonreciprocal component is the gyrator, which can be the building block of other nonreciprocal components, like ciculators and isolators. Spatiotemporally modulated (STM) gyrators are typically based on a pair of frequency converters with different modulation phases, connected through a linear time-invariant network. Such gyrators are usually designed to operate with a single modulation sideband. In this paper we argue that this approach is suboptimal and show how adding just one more sideband can increase the bandwidth by 40% with a lower modulation frequency and the same modulation amplitude. We present an implementation of the proposed approach based on a double-balanced circuit with Wheatstone bridges of varactors, which provides large isolation between the input signal and the sidebands. We provide a theoretical and an experimental analysis of the circuit with excellent agreement to each other. In addition to introducing a topology of STM gyrators with improved bandwidth compared with existing designs, our results highlight a potential connection between the bandwidth of STM devices and their harmonic order, which might also find applications in other STM systems, like isolators, circulators, and photonic topological insulators.

DOI: 10.1103/PhysRevApplied.18.044068

I. INTRODUCTION

Nonreciprocal devices are important in microwave and photonic systems for protection of sources from reflections, the design of full-duplex systems, and the design of quantum-computing systems. Conventional nonreciprocal devices are based on ferrites, which become gyrotropic when biased with static magnetic fields, but they tend to be bulky and are difficult to be incorporated in integrated circuit technologies [1,2]. For this reason, there has been a lot of interest in developing magnetless nonreciprocal devices. The two main approaches that have been proposed in this direction include devices based on transistors [3–6], and spatiotemporally modulated (STM) devices [7–23]. Transistor-based devices offer nonreciprocal responses over broad bandwidths, but they have limitations in terms of noise figure and power handling [24,25]. These hurdles are partially overcome with STM devices, at the expense of a usually smaller bandwidth.

The most fundamental nonreciprocal device is the gyrator, which exhibits a 180° phase difference for transmission in opposite directions. STM gyrators are typically based on cascaded frequency converters with different modulation phases [13,26–33]. The frequency converters can be in the form of time-modulated reactive elements or switches, and their role is to modify the phase of a signal as it is converted to other frequencies by amounts that are equal to the modulation phases. With the exception of a limited number of recent works [29,31,32], STM gyrators based on reactive elements are typically designed to operate via a single sideband and have limited bandwidths [1,26,28,30]. On the other hand, switched-based gyrators operate via a large number of sidebands and have broad bandwidths [15,33,34]. This fact suggests a possible connection between the bandwidth and harmonic index of STM devices, which could be used to expand their bandwidth without increasing their modulation parameters.

Here we show that the bandwidth of STM gyrators can be substantially expanded with the same modulation amplitude and a smaller modulation frequency by increasing their harmonic order, i.e., the number of sidebands that can propagate through them. We demonstrate this effect for a dual-sideband gyrator based on double-balanced mixers of varactors, and show that such a topology is ideal for the design of STM devices, because it provides large isolation between the input signal and the sidebands, without the need of filters. We provide a theoretical analysis for the

*dsounas@wayne.edu

circuit and present an experimental prototype at 1 GHz, with a response in very good agreement with the theory. Our analysis unveils a fundamental relation between the bandwidth and the harmonic order of STM devices, which can be important in the design of other STM devices, like circulators, isolators, and photonic topological insulators.

The paper is organized as follows. In Sec. II we present a general theoretical analysis for single- and dual-band gyrators and discuss the advantages of the latter with respect to the former in terms of the bandwidth. In Sec. III we present an implementation of a dual-band gyrator based on double-balanced mixers and present a theoretical analysis for it. Section IV presents the results of an experiment that validates the theory. Finally, in Sec. V we provide conclusions and possible future directions.

II. SINGLE- VERSUS DUAL-SIDEBAND GYRATORS

The simplest architecture of an STM gyrator comprises of two frequency converters connected through a linear network, as in Fig. 1(a). The converters are modulated with the same frequency but different phases. In principle, a network like this supports multiple sidebands $\omega \pm n\Omega$, where ω is the frequency of an input signal, Ω is the modulation frequency, and n an integer. However, in practice, the most significant sidebands are those of first order ($n = 1$), and higher-order ones are usually neglected. Furthermore, it is a common practice to design the circuit so that only one of the two first-order sidebands (i.e., either $n = 1$ or $n = -1$) is significantly excited and the other one is suppressed. Such selectivity is achieved, for example, by designing the linear network between the converters to exhibit a low impedance at one sideband and a high impedance at the other. A practical example of such a gyrator is shown in Fig. 1(b). In this circuit, the linear network between the converters is the series combination of the inductor L and the static capacitance of the varactors, and is a first-order band-pass filter. The inductors L_0 in series with the input and output ports are added to prevent the flow of the sidebands to the ports and achieve matching at frequency ω, and can be considered part of passive matching networks at the ports. The property of frequency converters that is important in the design of the gyrator is the transfer of the modulation phase to the converted signal. For example, the phases of the upper and lower sidebands after the first frequency converter in Fig. 1 are shifted from the phase of the input signal by ϕ_1 and $-\phi_1$, respectively. As these sidebands are transmitted through the second frequency converter and converted back to the original frequency ω, their phases experience an additional change of $-\phi_2$ and ϕ_2 for the upper and lower sideband, respectively. Then, a connection of two frequency converters with different modulation phases, as in Fig. 1, exhibits different transmission phases in opposite directions. Specifically, if ϕ is the phase of the linear network between the converters, the transmission phase from left to right and reverse is $\phi_{21} = \phi_1 + \phi - \phi_2$ and $\phi_{12} = \phi_2 + \phi - \phi_1$, respectively, for operation via the upper sideband, and $\phi_{21} = -\phi_1 + \phi + \phi_2$ and $\phi_{12} = -\phi_2 + \phi + \phi_1$ for operation via the lower sideband. As a result, transmission in opposite directions occurs with a phase difference $\phi_{21} - \phi_{12} = \pm 2(\phi_1 - \phi_2)$. For a gyrator, the phase difference is equal to π, leading to $\phi_1 - \phi_2 = \pm\pi/2$, i.e., a quadrature modulation for the frequency converters. Assuming that $\phi_1 = 0$ and $\phi_2 = -\pi/2$, the transmission coefficients in opposite directions take the form

$$S_{21}(\omega) = -S_{12}(\omega) = \pm jM^2 H(\omega \pm \Omega), \tag{1}$$

where M is the modulation amplitude and $H(\omega)$ is the frequency response of the linear network between the converters. For a linear network with a first-order band-pass response, as the circuit in Fig. 1(b),

$$H(\omega) = \frac{A}{\omega - \omega_0 - j\gamma}, \tag{2}$$

where ω_0 is the resonance frequency, γ the decay rate, and A a complex-valued constant. Replacing Eq. (2) into Eq. (1) gives

$$S_{21}(\omega) = -S_{12}(\omega) = \pm\frac{jM^2 A}{\omega \pm \Omega - \omega_0 - j\gamma}, \tag{3}$$

showing that the gyrator exhibits a band-pass response with a center frequency $\omega_0 - \Omega$ or $\omega_0 + \Omega$ for operation via the upper or lower sideband, respectively, and a bandwidth 2γ, equal to the bandwidth of $H(\omega)$. Assuming a power efficiency η^2, defined as the ratio between the transmitted and absorbed powers, and assuming a matched circuit at the center frequency, the transmission coefficients

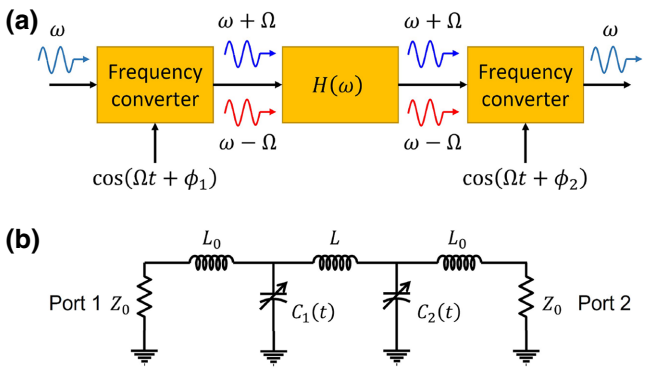

FIG. 1. (a) Generic architecture of an STM gyrator. (b) The most common circuit of STM gyrators.

become

$$S_{21}(\omega) = -S_{12}(\omega) = \pm e^{j\alpha}\frac{j\eta\gamma}{\omega - \omega_0 - j\gamma \pm \Omega}, \quad (4)$$

where α is a phase that depends on the linear network. Such phase can be absorbed in the definition of the ports and, therefore, will be taken equal to 0 from this point on. Equation (4) is in perfect agreement with the transmission coefficient found from the rigorous solution of the circuit in Fig. 1(b), as shown in Appendix A.

The preceding analysis is valid under the condition of a single-sideband excitation. This condition is satisfied for $\Omega \gg \gamma$, so that the input frequency bands that lead to upper and lower sidebands within the pass band of $H(\omega)$ do not overlap. For example, the upper sideband falls within the pass band of $H(\omega)$ for input frequencies

$$\omega_0 - \gamma - \Omega < \omega < \omega_0 + \gamma - \Omega. \quad (5)$$

For the lower sideband, this condition is

$$\omega_0 - \gamma + \Omega < \omega < \omega_0 + \gamma + \Omega. \quad (6)$$

To avoid overlapping between these bands, we need $\omega_0 + \gamma - \Omega < \omega - \gamma + \Omega$, which leads to $\Omega > \gamma$. The opposite case is Ω of the same order as γ, which would result in excitation of both sidebands, effectively creating two channels between the ports, and leading to a bandwidth increase. Each of these channels is characterized by a transmission coefficient as in Eqs. (1) and (4), resulting in a net transmission coefficient

$$S_{21}(\omega) = -S_{12}(\omega) = jM^2\big[H(\omega + \Omega) - H(\omega - \Omega)\big], \quad (7)$$

or

$$S_{21}(\omega) = -S_{12}(\omega) = -\frac{j2\eta\gamma\Omega}{(\omega - \omega_0 - j\gamma)^2 - \Omega^2}. \quad (8)$$

Apart from a difference in the phase, which can be cancelled via a shift of the reference planes of the ports, this expression is in perfect agreement with the transmission coefficient obtained through a rigorous solution of the circuit in Fig. 1 under dual-sideband operation (Appendix A). The modulus of the transmission coefficient is plotted in Fig. 2 against Ω/γ and $(\omega - \omega_0)/\gamma$. For $\Omega \gg \gamma$, the response consists of two separate pass bands centered at $\omega_0 \mp \Omega$ with a bandwidth 2γ. This regime corresponds to single-sideband excitation, as described above, and it could be used in the design of dual-band gyrators. As Ω decreases, these bands come closer to each other and, for $\Omega = \gamma$, they form a single band centered at ω_0 with a bandwidth $2\sqrt{2}\gamma$. Therefore, dual-sideband operation with $\Omega = \gamma$ leads to a 40% bandwidth increase with a smaller

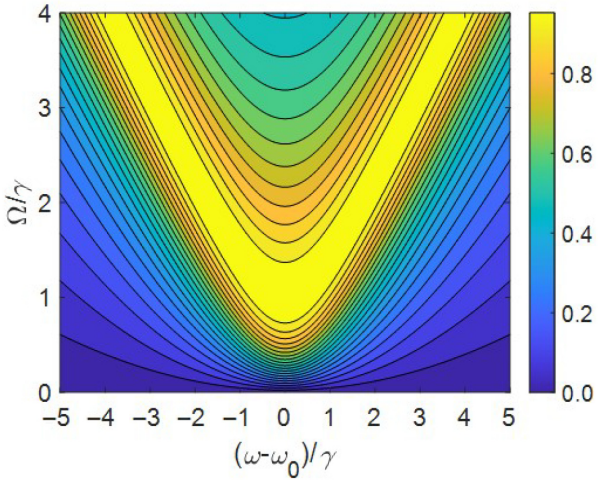

FIG. 2. Transmission coefficient $|S_{21}|$ against $(\omega - \omega_0)/\gamma$ and Ω/γ for a dual-sideband gyrator.

modulation frequency. For $\Omega = \gamma$, the square modulus of the transmission coefficient takes the form

$$|S_{21}(\omega)|^2 = \frac{4\eta\gamma^4}{(\omega - \omega_0)^4 + 4\gamma^4}, \quad (9)$$

which is the response of a second-order flat-top (Butterworth) filter. The existence of the second sideband effectively increases the order of the network and results in a broadening of its bandwidth. If Ω is further reduced to a value smaller than γ, there is a single transmission peak at ω_0 that decreases with decreasing Ω. We refer to this case as the subcritical regime.

III. DOUBLE-BALANCED GYRATOR

At first sight, the circuit in Fig. 1(b) might seem a good candidate for the design of a dual-sideband gyrator. However, it suffers from a significant drawback that prevents it of being used so. For dual-sideband operation, the branch between the varactors needs to exhibit a low impedance for both sidebands $\omega \pm \Omega$. Then, it will also exhibit a low impedance at the input frequency ω, establishing a direct path between the ports. Such a path would be reciprocal and would dilute the nonreciprocal response of the sidebands. A possible solution to this problem could consist of increasing the order of the filter between the varactors to achieve an impedance with zeros at $\omega \pm \Omega$ and a pole at ω. However, in addition to increasing the complexity of the circuit, such a solution would most definitely lead to a narrower bandwidth than for a single-sideband operation. This is probably the reason why the circuit in Fig. 1(b) has never been used in the dual-sideband regime, despite being known since the 1950s.

This problem can be overcome with the double-balanced circuit in Fig. 3, where varactors are replaced by differentially modulated Wheatstone bridges (double-balanced

mixers). Each bridge consists of four varactors with the same dc capacitance and a 180° modulation phase difference for the varactors on opposite sides. The input signal is differentially applied to terminals L and R, and the sidebands are collected from terminals B and U. The linear networks between the bridges are realized though parallel inductors, which together with the static capacitance of the bridges lead to first-order band-pass filters. The loss of the circuit is modeled through resistors in parallel with the inductors and accounts for the loss of both the varactors and the inductors. The advantage of this topology is that it provides isolation between the external (L and R) and internal (U and B) terminals without filters, by using the orthogonality of the modes at these terminals. The differential application of the input signal at L and R results in a virtual ground at B and U, preventing the flow of this signal to the internal branches of the circuit. For the same reason, L and R are virtual grounds for the signals flowing through the internal branches, preventing the flow of these signals to the external ports. The only way that the input signal and the sidebands can couple is through the modulation, which is applied in a differential manner to compensate the opposite parity of the input signal and the sidebands. In other words, with this architecture, coupling between the external and the internal branches is possible only through frequency conversion, making it ideal for dual-sideband operation.

By definition, a differential excitation means $V_{\rm L} = -V_{\rm R}$. This fact combined with the inversion symmetry of the circuit with respect to P [Fig. 3(b)] suggests that all voltages and currents have an odd inversion symmetry with respect to P. Specifically, the voltages at terminals U and B are opposite and the currents flow as in Fig. 3(b). Then, Kirchhoff's laws give

$$I_1(t) = C\frac{d}{dt}\Big[\big[1 + M\cos(\Omega t + \theta)\big]\big[V_{\rm L}(t) - V_{\rm U}(t)\big]\Big], \tag{10a}$$

$$I_2(t) = C\frac{d}{dt}\Big[\big[1 - M\cos(\Omega t + \theta)\big]\big[V_{\rm L}(t) + V_{\rm U}(t)\big]\Big]. \tag{10b}$$

The currents and voltages at the L/U ports are found as

$$I_{\rm L}(t) = I_1(t) + I_2(t) = 2C\frac{d}{dt}\big[V_{\rm L}(t) - d(t,\theta)V_{\rm U}(t)\big], \tag{11a}$$

$$I_{\rm U}(t) = I_2(t) - I_1(t) = 2C\frac{d}{dt}\big[V_{\rm U}(t) - d(t,\theta)V_{\rm L}(t)\big], \tag{11b}$$

where $d(t,\theta) \equiv M\cos(\Omega t + \theta)$ and θ is the modulation phase of the bridge (0°, −90°, 90°, and 0° for the top-left, top-right, bottom-left, and bottom-right bridges, respectively). Applying a Fourier transform to these equations,

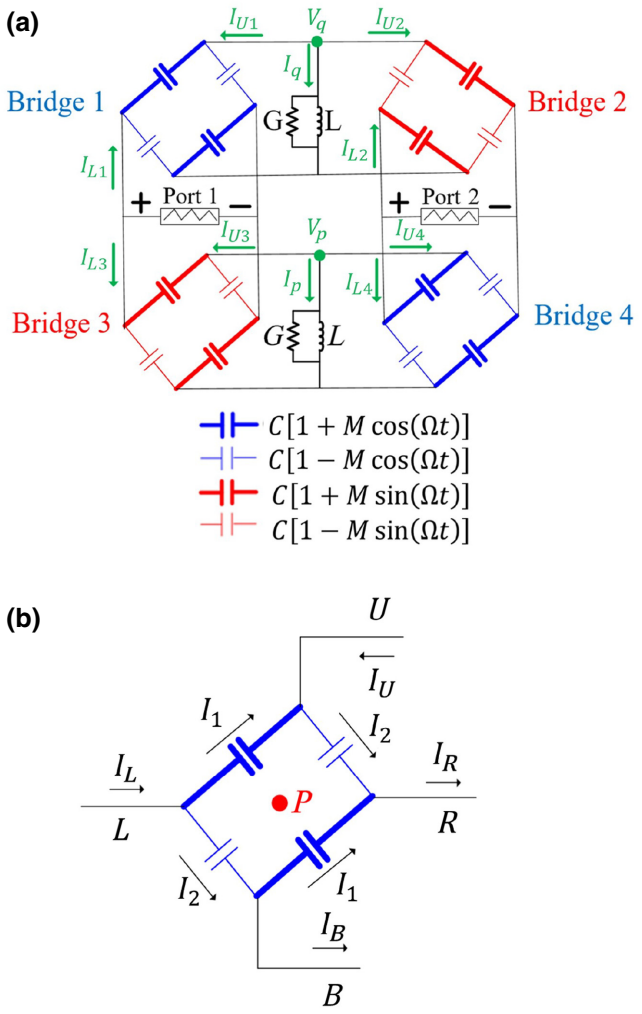

FIG. 3. (a) Double-balanced gyrator. (b) One bridge of the gyrator.

they are converted to

$$I_{\rm L}(\omega) = j2\omega C\Big[V_{\rm L}(\omega) - \frac{M}{2}e^{j\theta}V_{\rm U}(\omega - \Omega) - \frac{M}{2}e^{-j\theta}V_{\rm U}(\omega + \Omega)\Big], \tag{12a}$$

$$I_{\rm U}(\omega) = j2\omega C\Big[V_{\rm U}(\omega) - \frac{M}{2}e^{j\theta}V_{\rm L}(\omega - \Omega) - \frac{M}{2}e^{-j\theta}V_{\rm L}(\omega + \Omega)\Big]. \tag{12b}$$

Equations (12a) and (12b) indicate that signals at the L/R and U/B terminals have frequencies $\omega, \omega \pm 2\Omega, \ldots$ and $\omega \pm \Omega, \omega \pm 3\Omega$, respectively. However, by having two paths with a 90° modulation phase difference (paths consisting of bridges 1 and 2, and 3 and 4), the tones $\omega \pm 2\Omega, \ldots$ at the L/R ports and $\omega \pm 3\Omega, \ldots$ at the U/B ports are cancelled, leaving only frequencies ω and $\omega \pm \Omega$ at the

L/R and U/B ports, respectively. Combining Eq. (12) with the rest of the equations of the circuit, we can work a solution and find the following admittance matrix between the external ports (Appendix B):

$$\mathbf{Y}(\omega) = \begin{bmatrix} Y_1(\omega) & Y_2(\omega) \\ -Y_2(\omega) & Y_1(\omega) \end{bmatrix}. \tag{13}$$

Here

$$Y_1(\omega) = Y_s(\omega) + a_+(\omega) + a_-(\omega), \tag{14a}$$

$$Y_2(\omega) = j\left[a_+(\omega) - a_-(\omega)\right], \tag{14b}$$

$$a_\pm(\omega) = \frac{M^2C^2\omega(\omega \pm \Omega)}{Y(\omega \pm \Omega)}, \tag{14c}$$

$$Y_s(\omega) = j\,4\omega C, \tag{14d}$$

$$Y(\omega) = j\,2\omega C + \frac{1}{j\,\omega L} + G, \tag{14e}$$

where $Y_s(\omega)$ is the admittance of the branches connected to the ports, which, for the circuit in Fig. 3(b), depends only on the capacitance of the varactors. More generally, $Y_s(\omega)$ is the admittance of the matching networks connected to the ports. Here $Y(\omega)$ is the admittance of the parallel combination of the bridges, the inductors, and the resistors.

The S parameters can be found from the Y parameters as [35]

$$S_{11} = S_{22} = \frac{(Y_0 - Y_1)(Y_0 + Y_1) - Y_2^2}{(Y_0 + Y_1)^2 + Y_2^2}, \tag{15a}$$

$$S_{21} = -S_{12} = \frac{2Y_2Y_0}{(Y_0 + Y_1)^2 + Y_2^2}. \tag{15b}$$

For frequencies close to the resonance of the circuit, these expressions simplify as (Appendix B)

$$S_{11}(\omega) = -1 - j\,\frac{2\eta\gamma(\omega - \omega_0' - j\,\gamma)}{(\omega - \omega_0' - j\,\gamma)^2 - \Omega^2}e^{j\alpha}, \tag{16a}$$

$$S_{21}(\omega) = \frac{2\eta\gamma\Omega}{(\omega - \omega_0' - j\,\gamma)^2 - \Omega^2}e^{j\alpha}, \tag{16b}$$

where

$$\omega_0' = \omega_0 + \frac{\omega_0 M^2}{8\left(1 + \frac{1}{4Q_C^2}\right)} \tag{17}$$

is the resonance frequency when modulation is on, $\omega_0 = 1/\sqrt{2LC}$ is the resonance frequency when there is no modulation, $Q_C = Y_0/(2\omega_0 C)$ is the Q factor of the bridges with respect to the impedance of the ports, $\gamma = \gamma_i + \gamma_m$

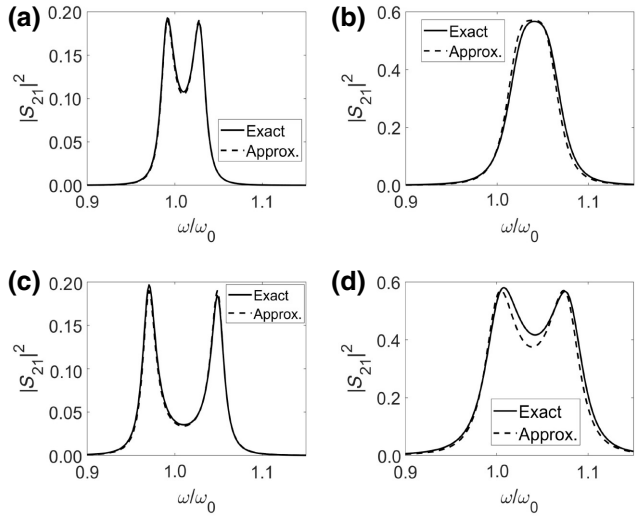

FIG. 4. Comparison between the exact and approximate formulas for S_{21} of the gyrator: (a) $M = 0.3$ and $\Omega = 0.02\omega_0$, (b) $M = 0.6$ and $\Omega = 0.02\omega_0$, (c) $M = 0.3$ and $\Omega = 0.04\omega_0$, (d) $M = 0.6$ and $\Omega = 0.04\omega_0$. In all cases, $\omega_0 = 2\pi$ GHz, $Z_0 = 50\ \Omega$, $C = 2$ pF, and $Q_i = \omega_0/(2\gamma_i) = 100$.

is the total decay rate, $\gamma_i = G/(4C)$ is the decay rate due to loss,

$$\gamma_m = \frac{\omega_0 M^2}{16Q_C\left(1 + \frac{1}{4Q_C^2}\right)} \tag{18}$$

is the radiative decay rate, $\eta = \gamma_m/\gamma$ is the efficiency, and $\alpha = 2\tan^{-1}[1/(2Q_e)]$. Note that $S_{21}(\omega)$ has the same form as Eq. (8) for the general model of a dual-sideband gyrator in Fig. 1. To validate Eq. (16), in Fig. 4 we compare the approximate S_{21} with the one obtained through the exact expressions (15) for various pairs of M and Ω. The agreement between the approximate and the exact results is very good in all cases.

Figure 5 plots the bandwidth $B = 2\sqrt{2}\gamma$, and S_{21} and S_{11} at the center frequency ω_0' against M for $\Omega = \gamma$ (flat-top condition), various C, $\omega_0 = 2\pi$ GHz, and a dissipation Q factor $Q_i = \omega_0/(2\gamma_i) = 100$. The transmission and bandwidth become maximum and the return loss becomes minimum for a capacitance about 1 pF. For this capacitance, a modulation amplitude of about 0.65 gives an insertion loss less than 1.5 dB and a bandwidth of about 10%. The optimum capacitance is one that leads to a maximization of η and γ_m. From the definition of the efficiency we have

$$\eta = \frac{\gamma_m}{\gamma} = 1 - \frac{\gamma_i}{\gamma_i + \gamma_m}, \tag{19}$$

from which we see that η is maximum when γ_m is maximum, which from Eq. (18) can be shown to happen for $Q_C = 1/2$. For $\omega_0 = 2\pi$ GHz and $Y_0 = 1/50$ S, this

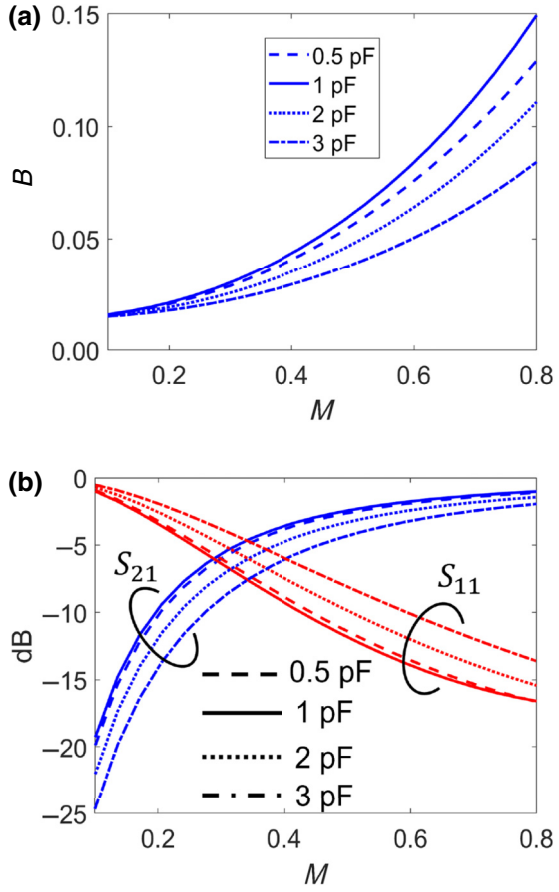

FIG. 5. (a) Bandwidth and (b) S_{21} and S_{11} at the center frequency versus M for different C, $\Omega = \gamma$ (flat-top response), $\omega_0 = 2\pi$ GHz, $Z_0 = 50\ \Omega$, and $Q_i = 100$.

condition gives $C = 0.8$ pF, close to the value determined from Fig. 5. For a flat-top response, the bandwidth is $B = 2\sqrt{2}\gamma = 2\sqrt{2}(\gamma_i + \gamma_m)$ and it is maximum also when γ_m is maximum. Figure 6 presents the S parameters of the gyrator versus frequency for an optimum capacitance, $M = 0.6$, $\Omega = \gamma$, and $Q_i = 100$, showing a flat-top response, as expected from theory.

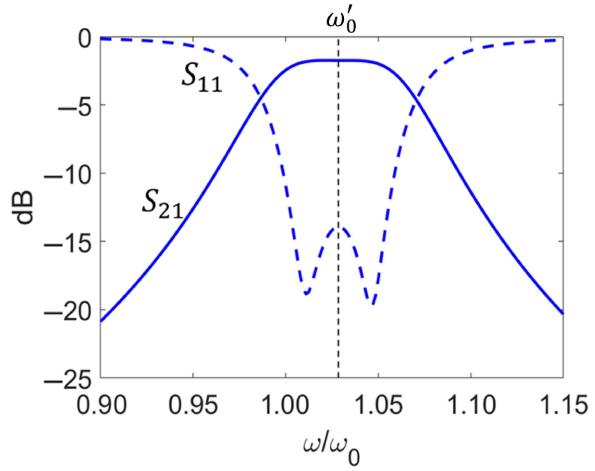

FIG. 6. The S parameters of the gyrator for $M = 0.6$, $\Omega = \gamma$, $C = 1$ pF, $\omega_0 = 2\pi$ GHz, $Z_0 = 50\ \Omega$, and $Q_i = 100$.

IV. SIMULATION AND MEASUREMENT RESULTS

Here we present simulation and measurement results of the circuit described in Sec. III. A schematic of the realized circuit is shown in Fig. 7. The bridges are made with varactors, specifically 1SV280 varactors by Toshiba. For the left- and right-hand side varactors of each bridge we use a common cathode connection, with the cathode at the L node in Fig. 3(b), while for the ones on the right-hand side we use a common anode connection, with the anode at the R node. Using an opposite polarity for opposite sides allows us to achieve a 180° phase difference in the modulation of the varactors with the same modulation signal. The dc signals for the biasing of the varactors are applied to the L and R nodes through large resistors that act as open circuits for the rf and modulation signals. A differential biasing scheme with two dc sources with opposite voltages is used, with the positive and negative voltages applied to the R and L nodes, respectively, to keep the varactors reverse biased. Since the varactors act as open circuits at

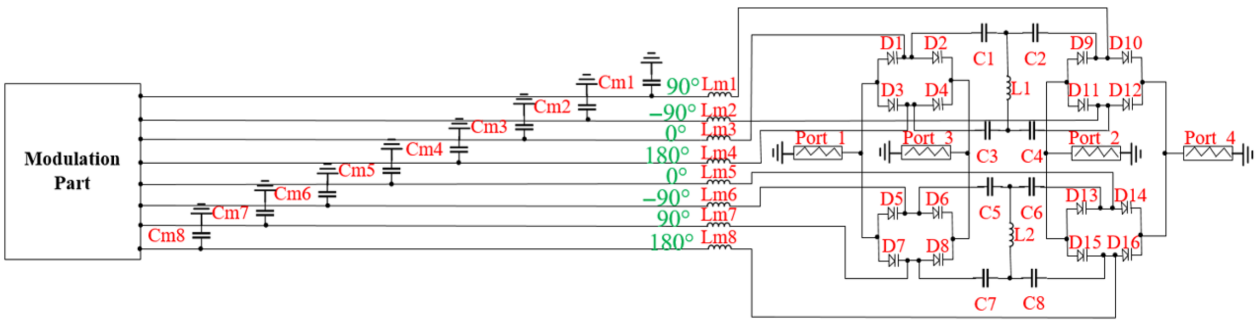

FIG. 7. The schematic of the proposed circuit.

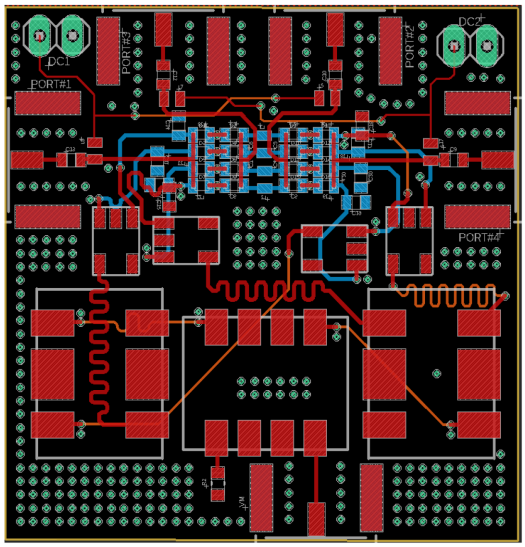

FIG. 8. Layout of the proposed circuit.

dc, all the dc voltage drops across them and the voltage drop across the biasing resistors is negligible, despite the large value of these resistors.

For the modulation of the varactors, we use one modulation source, the output of which is divided into eight equal parts with phases of 0°, 180°, or ±90°. Four of these signals are applied to the U nodes of the bridges and the other four to the B nodes. The phases of the first four signals are 0° and 90° for the top bridges from left to right and −90° and 0° for the bottom bridges in the same order. The other four signals (those applied to the B nodes) have phase differences of 180° with respect to the first four signals. The modulation signals are generated through a combination of 90° and 180° hybrids and baluns. Specifically, the output of the modulation source is split into four signals through a single 90° hybrid followed by two 180° hybrids. These signals are subsequently split into two equal parts with 180° phase differences through baluns, and are directed to the U and B nodes of the bridges. To reduce the coupling between the rf and modulation lines, low-pass filters are added in the path of the modulation network, taking

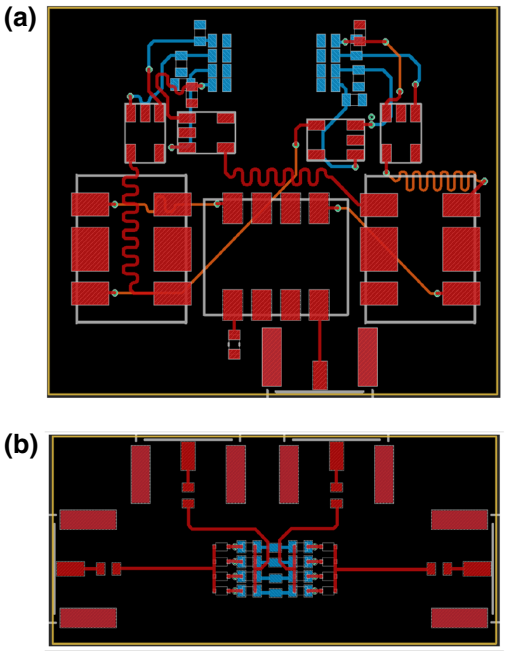

FIG. 9. (a) Modulation and (b) rf parts of the layout. Red and blue traces represent the top and bottom layers, respectively.

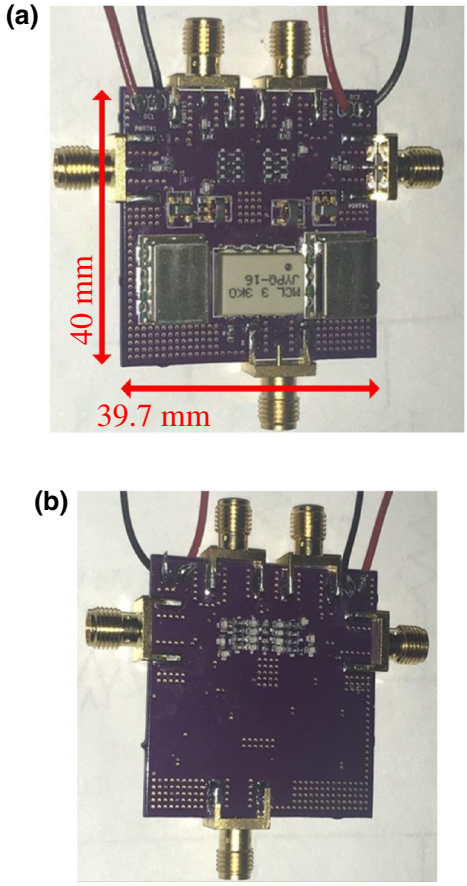

FIG. 10. (a) Top and (b) bottom layer of the fabricated prototype.

TABLE I. Lumped elements.

Element		**Value**
rf part	D	~ 2.12 pF @ $V_{dc} = 3$ V
	L	3.6 nH
	C	39 pF
	C_B	1000 pF
Modulation part	L_m	16 nH
	C_m	10 pF
dc part	R_B	10 kΩ

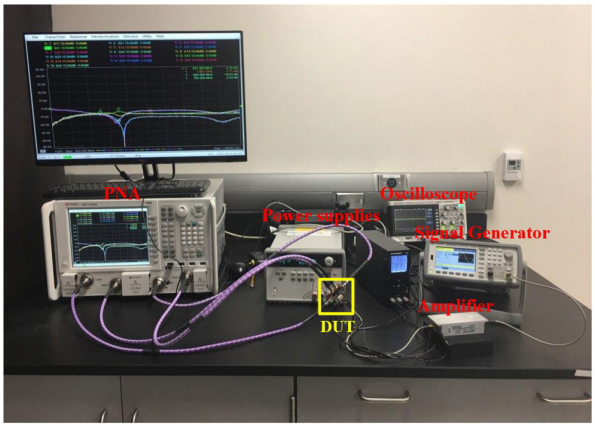

FIG. 11. Measurement setup.

TABLE II. Measurement equipment.

Part	Model	Quantity
Power supply	E3648A Keysight	1
PNA Microwave Network Analyzer	N5222A Keysight	1
Oscilloscope	DSOX1102A Keysight	1
Signal generator	33611A Keysight	1
Amplifier	ZHL-1-2W+ Minicircuits	1

into account that the modulation frequency is significantly smaller than the rf.

The rest of the circuit is as in Fig. 3, with an exception of eight additional capacitors in series with the lines between the bridges (C1–C8 in Fig. 7), the purpose of which is to provide isolation between the modulation signals at the right and left sides of the circuit. These capacitors act as high-pass filters and have a large enough value to block the modulation signals and transmit the rf ones. Such isolation capacitors are not necessary between the top and bottom bridges, due to the symmetry of the circuit and the differential character of the modulation, which renders the L and R nodes virtual grounds for the modulation signal, suppressing the coupling between the modulation signals of the top and bottom bridges and providing isolation between the modulation signals and the rf ports.

Based on the analysis in Sec. III we picked up a dc varactor capacitance of 3 pF and an interbridge inductance of 8.4 pF as a starting point for the design at 1 GHz. For the numerical analysis, we use ANSYS HFSS for full-wave simulations of the layout and Advanced Design System for circuit simulations based on the harmonic balance method. The layout, shown in Fig. 8, is designed on a four-layer FR4 substrate with $\epsilon_r = 3.66$, $\tan\delta = 0.012$, and a thickness of 0.17 mm. The top layer is used for the four varactor bridges and part of the modulation network, specifically the hybrids and the baluns. The bottom layer is used for the part of the circuit between the bridges, including the series capacitors and the shunted inductors, and the modulation filters. The middle layers are used for bypass lines, whenever it is necessary. All traces are realized as grounded coplanar waveguides. To avoid baluns, we added four rf ports and the differential S parameters are extracted

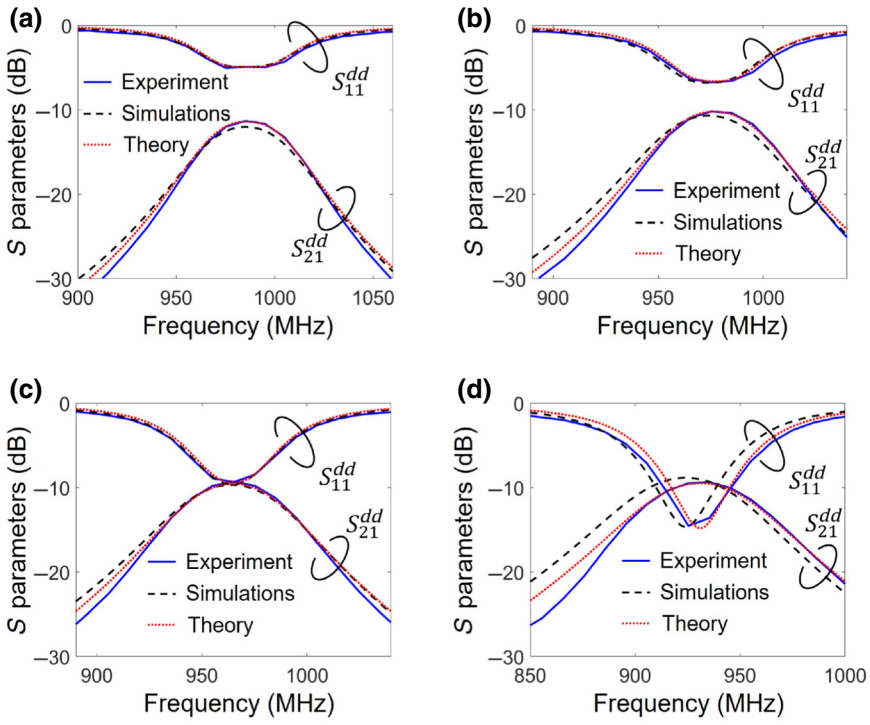

FIG. 12. Experimental, simulated and theoretical odd-mode S parameters for four different modulation power: (a) −8 dBm, (b) −7 dBm, (c) −6 dBm, (d) −5 dBm. The fitting parameters for the theoretical results are (a) $\omega_0' = 2\pi \times 986$ MHz, $\gamma_i = 105$ MHz, $\gamma_m = 45$ MHz, (b) $\omega_0' = 2\pi \times 977$ MHz, $\gamma_i = 105$ MHz, $\gamma_m = 58$ MHz, (c) $\omega_0' = 2\pi \times 965$ MHz, $\gamma_i = 110$ MHz, $\gamma_m = 78$ MHz, and (d) $\omega_0' = 2\pi \times 931$ MHz, $\gamma_i = 120$ MHz, $\gamma_m = 110$ MHz.

through a mixed-mode analysis as

$$S_{11}^{dd} = \frac{S_{11} - S_{13} - S_{31} + S_{33}}{2}, \tag{20a}$$

$$S_{22}^{dd} = \frac{S_{22} - S_{24} - S_{42} + S_{44}}{2}, \tag{20b}$$

$$S_{21}^{dd} = \frac{S_{21} - S_{23} - S_{41} + S_{43}}{2}, \tag{20c}$$

$$S_{12}^{dd} = \frac{S_{12} - S_{14} - S_{32} + S_{34}}{2}, \tag{20d}$$

where the superscript *dd* indicates differential parameters. For better visualization, Fig. 9 presents a breakdown of the layout into its modulation and rf parts, with red and blue traces representing the top and bottom layers, respectively. The top and bottom layers of the fabricated prototype are shown in Fig. 10. The values of the circuit's elements are listed in Table I, while the setup and the equipment used in the experiment are shown in Fig. 11 and Table II, respectively. Owing to the fact that the available power from the signal generator is limited, an amplifier is used to achieve the modulation signal level of 1 W required for the operation of the circuit.

The differential S parameters are presented in Fig. 12 for the measured prototype, simulations, and theory for four different modulation powers. For the simulation results, we use an inductance of 4.25 nH, slightly larger than the nominal value of the inductor on the fabricated board, to achieve good frequency alignment with the measured results. The dc and modulation voltages had also to be slightly tuned off their experimental values to compensate for uncertainties in the values of the lumped elements, especially the $C - V$ characteristic response of the varactors. The loss of the inductors in simulations is selected as 1 Ω, again to achieve good fitting with the experimental results. The theoretical results are obtained through Eq. (16) and the fitting to the experimental results is performed with respect to γ_i, ω_0', and γ_m. The fitting parameters values are given in the caption of Fig. 12. The experimental results show an increase in γ_m with the modulation power, which is consistent with Eq. (18), according to which γ_m is proportional to M^2, and, therefore, the modulation power. From this model, one would expect γ_m to increase proportionally to the modulation power. This is mostly true for the values of γ_m in Fig. 12. For example, between Figs. 12(a) and 12(b), γ_m increases by a factor of 1.3 compared with the modulation power that increases by a factor of 1.26. Deviations from this trend, which become more pronounced at large modulation powers, are attributed to higher-order nonlinear effects in the varactors that result in a nonlinear dependence between M^2 and the modulation power. It can also be noted that γ_i increases slightly with increasing modulation power, with a possible explanation being the driving of the varactor into the forward biasing regime, which would create a resistive component in its response.

The agreement between the experimental, simulated, and theoretical results is very good in all cases. The S parameters show a single peak in the transmission coefficient, indicating operation in the subcritical regime $\Omega < \gamma$. The fitting of the theoretical expressions to the experimental results reveals an intrinsic decay rate in the order of 105 MHz ($Q_i \approx 30$), larger than what was anticipated during the design of the circuit from the manufacturer-given loss parameters of the components. Such γ_i is larger than the modulation frequency $\Omega = 2\pi \times 15 = 94$ MHz explaining the subcritical response in the measured results. For a flat-top response, the modulation frequency would need to be equal to γ. Assuming a modulation amplitude $M = 0.6$ and an optimum $Q_C = 1/2$ for maximum efficiency and bandwidth, $\gamma = 246$ MHz and a flat-top response would require a modulation frequency of 40 MHz. The transmission coefficient in such a case, calculated through Eq. (16), and would be in the order of −5 dB. Achieving higher transmission would require components (varactors or inductors) with lower loss. In agreement with theory, the results in Fig. 12 show an increase of the transmission coefficient as the modulation power increases. Furthermore, they reveal a red shift in the resonance frequency

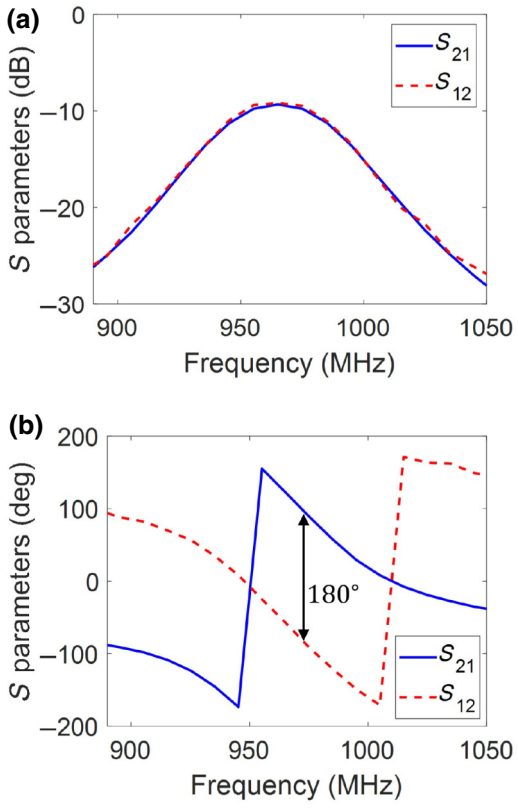

FIG. 13. Amplitude and phase of the odd-mode S parameters for a modulation power of −6 dBm.

with increasing modulation. Such an effect, which is in fact opposite than what is expected from Eq. (17), is attributed to an increasing dc capacitance for the varactors with an increasing modulation, and is the result of the second-order nonlinear response of the varactors [10]. Finally, to verify that the circuits provide the response of a gyrator, Fig. 13 presents the amplitude and phase of S_{21}^{dd} and S_{12}^{dd}. In agreement with the theory, S_{21}^{dd} and S_{12}^{dd} have the same amplitude and a phase difference of 180° over the entire frequency band of the measurement.

V. CONCLUSION

In this paper we present STM gyrators with dual-sideband operation, leading to a larger bandwidth and a lower modulation frequency than the conventional single-sideband STM gyrators. We present an implementation of the proposed gyrators based on a double-balanced topology that provides isolation between the external and internal branches of the gyrator without filters. We measure this circuit and obtain an excellent agreement with theory and simulations. More broadly, the presented analysis points into a direction for increasing the bandwidth of reactive STM devices by increasing the number of sidebands that can be transmitted in the circuit, and it can find applications in the design of other STM devices, like isolators, circulators, and photonic topological insulators.

APPENDIX A: GENERIC MODEL OF AN STM GYRATOR

To get a deeper understanding of the properties of STM gyrators, we use the simple model in Fig. 14. The modulation of the varactors is given by

$$C_i(t) = C_0 + MC_0\cos(\Omega t + \phi_i), \tag{A1}$$

where C_0 is the static capacitance, M the modulation amplitude, Ω the modulation frequency, and ϕ_i the modulation phase. The input signal coming from the ports has frequency ω. The circuit is designed so that the branches in series with the ports allow flow of signals with frequency ω, while the branches between the varactors allow flow of signals with frequencies $\omega+\Omega$ or $\omega-\Omega$. The frequency selectivity of the branches is achieved by designing them to exhibit a low impedance at the allowed frequency and a high impedance at other frequencies. For example, the inductor L_s in series with the ports is selected so that together with the capacitance of the varactors provides a low impedance at ω and a high one at $\omega+\Omega$ or $\omega-\Omega$. Similarly, the inductor L between the varactors is selected so that together with the capacitances of the varactors it provides a low impedance at $\omega+\Omega$ or $\omega-\Omega$ and a high one at ω.

Assume now that the circuit is designed to operate via the upper sideband $\omega+\Omega$. If voltages and currents are

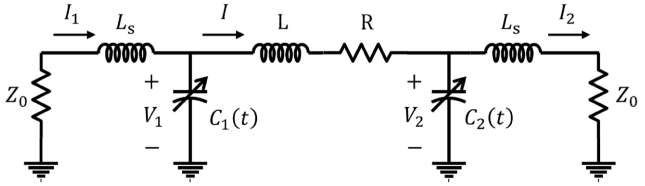

FIG. 14. A simple model for an STM gyrator.

defined as in Fig. 14, the varactors satisfy the equations [1]

$$\begin{bmatrix} V_1(\omega) \\ V_1(\omega+\Omega) \end{bmatrix} = \mathbf{M}_1(\omega)\begin{bmatrix} I_1(\omega) \\ -I(\omega+\Omega) \end{bmatrix}, \tag{A2a}$$

$$\begin{bmatrix} V_2(\omega) \\ V_2(\omega+\Omega) \end{bmatrix} = \mathbf{M}_2(\omega)\begin{bmatrix} I_2(\omega) \\ I(\omega+\Omega) \end{bmatrix}, \tag{A2b}$$

where

$$\mathbf{M}_i(\omega) = \begin{bmatrix} \frac{1}{j\omega C_0'} & \frac{-Me^{-j\phi_i}}{j\omega C_0'} \\ \frac{-Me^{j\phi_i}}{j(\omega+\Omega)C_0'} & \frac{1}{j(\omega+\Omega)C_0'} \end{bmatrix}, \tag{A3}$$

and $C_0' = (1-M^2)C_0$. Using these equations we can solve the circuit for the voltages and current at the ports and obtain the following impedance matrix:

$$\mathbf{Z}(\omega) = \begin{bmatrix} Z_1(\omega) & Z_2(\omega)e^{-j\Delta\phi} \\ Z_2(\omega)e^{j\Delta\phi} & Z_1(\omega) \end{bmatrix}. \tag{A4}$$

Here

$$Z_1(\omega) = Z_s(\omega) + a_+(\omega), \tag{A5a}$$

$$Z_2(\omega) = -a_+(\omega). \tag{A5b}$$

$Z_s(\omega) = j\omega L_s + 1/(j\omega C_0')$ is the impedance of the branches in series with the ports,

$$a_+(\omega) = \frac{M^2}{\omega(\omega+\Omega)C_0'^2 Z(\omega+\Omega)}, \tag{A6}$$

$\Delta\phi = \phi_1 - \phi_2$, and

$$Z(\omega) = R + j\omega L + \frac{2}{j\omega C_0'} \tag{A7}$$

is the impedance of the branch between the varactors. The S parameters can be found from the impedance matrix

as [35]

$$S_{21}(\omega) = \frac{2Z_0 Z_2(\omega) e^{j\,\Delta\phi}}{\left[Z_1(\omega)+Z_0\right]^2 - \left[Z_2(\omega)\right]^2}, \tag{A8a}$$

$$S_{12}(\omega) = \frac{2Z_0 Z_2(\omega) e^{-j\,\Delta\phi}}{\left[Z_1(\omega)+Z_0\right]^2 - \left[Z_2(\omega)\right]^2}. \tag{A8b}$$

Applying Eq. (A5) to these equations gives

$$S_{21}(\omega) = -\frac{2Z_0 a_+(\omega) e^{j\,\Delta\phi}}{[Z_s(\omega)+Z_0][Z_s(\omega)+Z_0+2a_+(\omega)]}, \tag{A9a}$$

$$S_{12}(\omega) = -\frac{2Z_0 a_+(\omega) e^{-j\,\Delta\phi}}{[Z_s(\omega)+Z_0][Z_s(\omega)+Z_0+2a_+(\omega)]}. \tag{A9b}$$

It is not difficult to show from Eq. (A9) that in the case of zero loss, i.e., $R = 0$, the network exhibits unitary transmission at a frequency ω where $Z_s(\omega) = 0$ and $Z(\omega + \Omega) = 0$. From $Z(\omega + \Omega) = 0$, this frequency is found as $\omega_0 - \Omega$, where $\omega_0 = \sqrt{2/(LC_0')}$. Therefore, the network exhibits a pass band centered at $\omega_0' = \omega_0 - \Omega$. The situation is not expected to change drastically in the case of low loss, apart from a reduction in the peak transmission at the center of the pass band. Within the pass band, $Z_s(\omega)$ can be taken approximately equal to zero, if the bandwidth $2\Delta\omega$ satisfies the condition

$$\frac{2\Delta\omega}{\omega_0'} \ll \omega_0' Z_0 C_0'. \tag{A10}$$

In such a case, Eq. (A8) simplify to

$$S_{21}(\omega) = -\frac{2a_+(\omega)}{2a_+(\omega)+Z_0} e^{j\,\Delta\phi}, \tag{A11a}$$

$$S_{12}(\omega) = -\frac{2a_+(\omega)}{2a_+(\omega)+Z_0} e^{-j\,\Delta\phi}. \tag{A11b}$$

To further simplify these expressions, we analyze them in terms of their poles. To find the poles, we solve $2a_+(\omega) + Z_0 = 0$, which can be written in the form

$$A(\omega) = 2M^2 + \omega(\omega+\Omega) C_0'^2 Z(\omega+\Omega) Z_0 = 0. \tag{A12}$$

We can see from this equation that in the absence of modulation ($M = 0$ and $\Omega = 0$), the resonances are the zeros of $Z(\omega)$, given by $\tilde{\omega}_0 = \pm\sqrt{\omega_0^2 - \gamma_i^2} + j\,\gamma_i$, where $\gamma_i = R/(2L)$. For low loss, i.e., $\gamma_i \ll \omega_0$, this frequency becomes $\tilde{\omega}_0 = \pm\omega_0 + j\,\gamma_i$. With modulation on, the resonance frequency is shifted by an amount that depends on M^2 and Ω. To the lowest order with respect to M^2 and Ω, the change in the resonance frequency can be found through a perturbative approach. Specifically, if $f(x)$ and $g(\epsilon_1, \ldots, \epsilon_N, x)$ are regular functions of x and ϵ_i at $x = x_0$ and $\epsilon_i = 0$, x_0 is a zero of $f(x)$, and $g(0, \ldots, 0, x) = 0$ for all x, the equation

$$f(x) + g(\epsilon_1, \ldots, \epsilon_N, x) = 0 \tag{A13}$$

has a solution

$$x = x_0 + \frac{1}{f'(x_0)} \sum_i \frac{\partial g(0, \ldots, 0, x_0)}{\partial \epsilon_i} \epsilon_i + \ldots, \tag{A14}$$

with the dots indicating terms of order higher than 1 in ϵ_i. Applying Eq. (A14) to Eq. (A12) and dropping terms of order higher than 1 in R as well as terms proportional to $M^2 R$ or ΩR, we find that the resonances of the circuit are given by

$$\tilde{\omega}_0' = \pm\omega_0 - \Omega + j\,\gamma, \tag{A15}$$

where $\gamma = \gamma_i + \gamma_m$ and

$$\gamma_m = \frac{M^2}{2Z_0 C_0'}. \tag{A16}$$

Here γ_m is the decay rate due to coupling between the middle branch and the ports induced by the modulation. Extracting the residue of $A(\omega)$ at $\tilde{\omega}_0'$ we can approximate $A(\omega)$ in the vicinity of $\tilde{\omega}_0'$ as $A(\omega) \approx j\,2Z_0 C_0(\omega - \omega_0 - j\,\gamma + \Omega)$. Inserting this approximation into Eq. (A11) gives

$$S_{21}(\omega) = \frac{j\,\eta\gamma}{\omega - \omega_0 - j\,\gamma + \Omega} e^{j\,\Delta\phi}, \tag{A17a}$$

$$S_{12}(\omega) = \frac{j\,\eta\gamma}{\omega - \omega_0 - j\,\gamma + \Omega} e^{-j\,\Delta\phi}, \tag{A17b}$$

where $\eta = \gamma_m/\gamma$ is the efficiency of the circuit, i.e., the ratio between the radiative and total decay rates. Equation (A17) validates the existence of a pass band with a center frequency $\omega_0 - \Omega$, in agreement with the previous discussion. The bandwidth of the pass band is 2γ and needs to satisfy Eq. (A10) for Eq. (A17) to be valid over the entire pass band. If $R \ll Z_0$, as is the case for low-loss components, the bandwidth condition is equivalent to $M \ll \omega_0' Z_0 C_0'$, and, considering that $M < 1$, it is satisfied for $\omega_0' Z_0 C_0' \gg 1$, i.e., varactors with impedances significantly smaller than the port impedance. The solution for operation via the lower sideband can be obtained from Eq. (A17) by replacing $\omega + \Omega$ with $\omega - \Omega$ and $\Delta\phi$ with $-\Delta\phi$.

The preceding analysis is valid for a sufficiently high Ω so that $Z(\omega_0' - \Omega) = 0$ or $Z(\omega_0' + \Omega) = 0$, and $Z(\omega_0)$ is very large. The condition of a large $Z(\omega_0)$ is necessary to prevent direct transmission of the input frequency from one port to the other, which would dilute the nonreciprocal response of the network [36]. This fact in principle precludes dual-sideband operation for the circuit in Fig. 14,

since in a dual-band operation it would be necessary that both $Z(\omega_0' - \Omega)$ and $Z(\omega_0' + \Omega)$ are close to zero, which would also entail a low value for $Z(\omega_0')$, leading to a direct path between the ports [37]. A solution to this problem is possible with the double-balanced architecture, but for the sake of understanding the physics of dual-sideband operation, we ignore the problem for a moment and analyze the circuit in Fig. 14 as if there is no direct path between the ports. In other words, we assume that there is some way for the circuit in Fig. 14 to allow flow of $\omega \pm \Omega$ only through the middle branch, and of ω only through the external branches. In such a case, the voltage and current vectors in Eq. (A2) would have to be modified to include the voltages and currents at both sidebands, and Eq. (A3) would become

$$\mathbf{M}_i(\omega) = \begin{bmatrix} \frac{1}{j\omega C_0'} & \frac{-Me^{-j\phi_i}}{j\omega C_0'} & \frac{-Me^{j\phi_i}}{j\omega C_0'} \\ \frac{-Me^{j\phi_i}}{j(\omega+\Omega)C_0'} & \frac{1}{j(\omega+\Omega)C_0'} & 0 \\ \frac{-Me^{-j\phi_i}}{j(\omega-\Omega)C_0'} & 0 & \frac{1}{j(\omega-\Omega)C_0'} \end{bmatrix}. \tag{A18}$$

Through a similar analysis as for the case of a single sideband, the impedance matrix between the ports is found as

$$\mathbf{Z}(\omega) = Z_s(\omega)\mathbf{I} + \mathbf{Z}_+(\omega) + \mathbf{Z}_-(\omega), \tag{A19}$$

where $\mathbf{I}$ is the identity matrix and

$$\mathbf{Z}_\pm(\omega) = \begin{bmatrix} a_\pm(\omega) & -a_\pm(\omega)e^{\mp j\,\Delta\phi} \\ -a_\pm(\omega)e^{\pm j\,\Delta\phi} & a_\pm(\omega) \end{bmatrix}. \tag{A20}$$

The S parameters can be found again from the impedance matrix. A specific case that leads to particularly convenient formulas for the S parameters, which is also the most important case in practice, is $\Delta\phi = \pm\pi/2$. In this case it can be shown that

$$S_{21}(\omega) = -\frac{2Z_0 a_+(\omega)e^{j\frac{\pi}{2}}}{[Z_s(\omega)+Z_0][Z_s(\omega)+Z_0+2a_+(\omega)]}, \\ -\frac{2Z_0 a_-(\omega)e^{-j\frac{\pi}{2}}}{[Z_s(\omega)+Z_0][Z_s(\omega)+Z_0+2a_-(\omega)]}, \tag{A21}$$

and $S_{12}(\omega) = -S_{21}(\omega)$. The transmission coefficients in this equation are the sum of the transmission coefficients for single-sideband operation over the upper or lower sidebands. Writing Eq. (A21) in terms of the transmission coefficients in Eq. (A17) we find that

$$S_{21}(\omega) = \frac{2\eta\gamma\Omega}{(\omega - \omega_0 - j\gamma)^2 - \Omega^2}. \tag{A22}$$

This expression shows that a dual-band gyrator exhibits the same response as a second-order band-pass filter, in contrast to a single-band gyrator that follows the response of a first-order band-pass filter. Therefore, a dual-band operation is expected to lead to a larger bandwidth than a single-band operation. Specifically, for $\Omega = \gamma$, the bandwidth of the dual-band gyrator is $2\gamma\sqrt{2}$, which is about 40% larger than the bandwidth of a single-band gyrator.

APPENDIX B: DOUBLE-BALANCED GYRATOR

To solve the circuit in Fig. 3(b), we define the auxiliary variables

$$V^\pm = \frac{V_q \mp jV_p}{\sqrt{2}}, \tag{B1a}$$

$$I_1^\pm = \frac{I_{U1} \mp jI_{U3}}{\sqrt{2}}, \tag{B1b}$$

$$I_2^\pm = \frac{I_{U2} \mp jI_{U4}}{\sqrt{2}}, \tag{B1c}$$

$$I^\pm = \frac{I_q \mp jI_p}{\sqrt{2}}. \tag{B1d}$$

Taking into account these definitions, the fact that $V_{U1} = V_{U2} = V_q$, $V_{U3} = V_{U4} = V_p$, $V_{L1} = V_{L3} = V_1$, and $V_{L2} = V_{L4} = V_2$, and applying Eqs. (12a) and (12b) for each bridge, we find that

$$I_1^+(\omega) = j\,2\omega CV^+(\omega) - j\sqrt{2}\omega MCV_1(\omega+\Omega), \tag{B2a}$$

$$I_1^-(\omega) = j\,2\omega CV^-(\omega) - j\sqrt{2}\omega MCV_1(\omega-\Omega), \tag{B2b}$$

$$I_2^+(\omega) = j\,2\omega CV^+(\omega) - \sqrt{2}\omega MCV_2(\omega+\Omega), \tag{B2c}$$

$$I_2^-(\omega) = j\,2\omega CV^-(\omega) + \sqrt{2}\omega MCV_2(\omega-\Omega). \tag{B2d}$$

The currents at the external ports are given by $I_1 = I_{L1} + I_{L3}$ and $I_2 = I_{L2} + I_{L4}$. Applying Eqs. (12a) and (12b) to these equations, we find that

$$I_1(\omega) = j\,4\omega CV_1(\omega) - j\sqrt{2}\omega MCV^+(\omega-\Omega) \\ - j\sqrt{2}M\omega CV^-(\omega-\Omega), \tag{B3a}$$

$$I_2(\omega) = j\,4\omega CV_2(\omega) + \sqrt{2}\omega MCV^+(\omega-\Omega) \\ - \sqrt{2}\omega MCV^-(\omega-\Omega), \tag{B3b}$$

Furthermore, we have the equations

$$I^\pm(\omega) + I_1^\pm(\omega) + I_2^\pm(\omega) = 0, \tag{B4}$$

$$I^\pm(\omega) = 2\left(G + \frac{1}{j\omega L}\right)V^\pm(\omega), \tag{B5}$$

for the voltages and currents of the parallel combinations of inductors and resistors between the bridges. The system of Eqs. (B3a)–(B2d), (B4), and (B5) is solved for I_1 and I_2,

giving

$$\begin{bmatrix} I_1(\omega) \\ I_2(\omega) \end{bmatrix} = \begin{bmatrix} Y_1(\omega) & Y_2(\omega) \\ -Y_2(\omega) & Y_1(\omega) \end{bmatrix} \begin{bmatrix} V_1(\omega) \\ V_2(\omega) \end{bmatrix}, \tag{B6}$$

where

$$Y_1(\omega) = Y_s(\omega) + a_+(\omega) + a_-(\omega), \tag{B7a}$$

$$Y_2(\omega) = j\left[a_+(\omega) - a_-(\omega)\right], \tag{B7b}$$

$$a_\pm(\omega) = \frac{M^2C^2\omega(\omega \pm \Omega)}{Y(\omega \pm \Omega)}, \tag{B7c}$$

$$Y_s(\omega) = j\,4\omega C, \tag{B7d}$$

$$Y(\omega) = j\,2\omega C + \frac{1}{j\,\omega L} + G. \tag{B7e}$$

The S parameters can be found from the Y parameters as [35]

$$S_{11} = S_{22} = \frac{(Y_0 - Y_1)(Y_0 + Y_1) - Y_2^2}{(Y_0 + Y_1)^2 + Y_2^2}, \tag{B8a}$$

$$S_{21} = -S_{12} = \frac{2Y_2Y_0}{(Y_0 + Y_1)^2 + Y_2^2}. \tag{B8b}$$

By replacing Y_1 and Y_2 from Eqs. (B7a) and (B7b) into these equations we can factorize them as

$$S_{11} = S_{22} = \frac{1}{2}\frac{-Y_+ + Y_0}{Y_+ + Y_0} + \frac{1}{2}\frac{-Y_- + Y_0}{Y_- + Y_0}, \tag{B9a}$$

$$S_{21} = -S_{12} = \frac{j\,2Y_0a_+}{(Y_0 + Y_s)(Y_0 + Y_+)} - \frac{j\,2Y_0a_-}{(Y_0 + Y_s)(Y_0 + Y_-)}, \tag{B9b}$$

where

$$Y_+(\omega) = Y_s(\omega) + 2a_+(\omega), \tag{B10a}$$

$$Y_-(\omega) = Y_s(\omega) + 2a_-(\omega). \tag{B10b}$$

To simplify Eq. (B9b), we follow a similar analysis as for the circuit in Fig. 14 in Appendix A except that now we keep $Y_s(\omega)$. The S parameters found through such analysis are

$$S_{11}(\omega) = -1 - j\,\frac{2\eta\gamma(\omega - \omega_0' - j\,\gamma)}{(\omega - \omega_0' - j\,\gamma)^2 - \Omega^2}e^{j\,\alpha}, \tag{B11a}$$

$$S_{21}(\omega) = \frac{2\eta\gamma\Omega}{(\omega - \omega_0' - j\,\gamma)^2 - \Omega^2}e^{j\,\alpha}, \tag{B11b}$$

where

$$\omega_0' = \omega_0 + \frac{\omega_0M^2}{8\left(1 + \frac{1}{4Q_C^2}\right)} \tag{B12}$$

is the resonance frequency when modulation is on, $\omega_0 = 1/\sqrt{2LC}$ is the resonance frequency when there is no modulation, $Q_C = Y_0/(2\omega_0C)$ is the Q factor of the bridges with respect to the impedance of the ports, $\gamma = \gamma_i + \gamma_m$ is the total decay rate, $\gamma_i = G/(4C)$ is the decay rate due to loss,

$$\gamma_i = \frac{\omega_0M^2}{16Q_C\left(1 + \frac{1}{4Q_C^2}\right)} \tag{B13}$$

is the radiative decay rate, and $\eta = \gamma_m/\gamma$ is the efficiency.

[1] R. E. Collin, *Foundations for Microwave Engineering* (John Wiley & Sons, New York, NY, 2007).

[2] J. D. Adam, L. E. Davis, G. F. Dionne, E. F. Schloemann, and S. N. Stitzer, Ferrite devices and materials, IEEE Trans. Microw. Theory Techn. **50**, 721 (2002).

[3] S. Tanaka, N. Shimimura, and K. Ohtake, Active circulators–The realization of circulators using transistors, Proc. IEEE **53**, 260 (1965).

[4] Y. Ayasli, Field effect transistor circulators, IEEE Trans. Magn. **25**, 3242 (1989).

[5] A. W. Keen, J. L. Glover, and R. J. Harris, Realisation of the circulator concept using differential-input operational amplifiers, Electron. Lett. **4**, 389 (1968).

[6] T. Kodera, D. L. Sounas, and C. Caloz, Magnetless nonreciprocal metamaterial (MNM) technology: Application to microwave components, IEEE Trans. Microw. Theory Tech. **61**, 1030 (2013).

[7] Z. Yu and S. Fan, Complete optical isolation created by indirect interband photonic transitions, Nat. Photon. **3**, 91 (2009).

[8] S. Qin, Q. Xu, and Y. E. Wang, Nonreciprocal components with distributedly modulated capacitors, IEEE Trans. Microw. Theory Techn. **62**, 2260 (2014).

[9] N. A. Estep, D. L. Sounas, and A. Alù, Magnetless microwave circulators based on spatiotemporally modulated rings of coupled resonators, IEEE Trans. Microw. Theory Techn. **64**, 502 (2016).

[10] A. Kord, D. L. Sounas, and A. Alù, Pseudo-linear time-invariant magnetless circulators based on differential spatiotemporal modulation of resonant junctions, IEEE Trans. Microw. Theory Techn. **66**, 2731 (2018).

[11] S. Keshavarz, H. M. Kadry, and D. L. Sounas, Four-port Spatiotemporally Modulated Circulator with Low Modulation Frequency, 2021 IEEE Texas Symposium on Wireless and Microwave Circuits and Systems (WMCS), 1 (2021).

[12] N. Reiskarimian and H. Krishnaswamy, Magnetic-free nonreciprocity based on staggered commutation, Nat. Commun. **7**, 11217 (2016).

[13] T. Dinc, M. Tymchenko, A. Nagulu, D. Sounas, A. Alù, and H. Krishnaswamy, Synchronized conductivity modulation to realize broadband lossless magnetic-free non-reciprocity, Nat. Commun. **8**, 795 (2017).

[14] A. Nagulu, A. Alù, and H. Krishnaswamy, in *Proc. IEEE Radio Freq. Integr. Circuits Symp. (RFIC)* (Philadelphia, Pennsylvania, 2018), p. 104.

[15] Y. Yu, G. Michetti, M. Pirro, A. Kord, D. L. Sounas, Z. Xiao, C. Cassella, A. Alù, and M. Rinaldi, Radio frequency magnet-free circulators based on spatiotemporal modulation of surface acoustic wave filters, IEEE Trans. Microw. Theory Techn., 4773 (2019).

[16] C. Cassella, G. Michetti, M. Pirro, Y. Yu, A. Kord, D. L. Sounas, A. Alú, and M. Rinaldi, Radio frequency angular momentum biased quasi-lti nonreciprocal acoustic filters, IEEE Trans. Ultrason. Ferroelectr. Freq. Control **66**, 1814 (2019).

[17] C. Yang and P. Gui, 85–110-GHz CMOS magnetic-free nonreciprocal components for full-duplex transceivers, IEEE J. Solid-State Circuits **54**, 368 (2019).

[18] Y. Hadad, J. C. Soric, and A. Alù, Breaking temporal symmetries for emission and absorption, Proc. Natl. Acad. Sci. **113**, 3471 (2016).

[19] L. Ranzani and J. Aumentado, Circulators at the quantum limit: Recent realizations of quantum-limited superconducting circulators and related approaches, IEEE Microw. Mag. **20**, 112 (2019).

[20] J. Zang, A. Alvarez-Melcon, and J. Gomez-Diaz, Nonreciprocal Phased-Array Antennas, Phys. Rev. Appl. **12**, 054008 (2019).

[21] Z. Wu, C. Scarborough, and A. Grbic, Space-Time-Modulated Metasurfaces with Spatial Discretization: Free-Space N-Path Systems, Phys. Rev. Appl. **14**, 064060 (2020).

[22] S. Taravati and C. Caloz, Mixer-duplexer-antenna leaky-wave system based on periodic space-time modulation, IEEE Trans. Antennas Propag. **65**, 442 (2017).

[23] A. Kord, D. L. Sounas, and A. Alù, Microwave nonreciprocity, Proc. IEEE **108**, 1728 (2020).

[24] G. Carchon and B. Nanwelaers, Power and noise limitations of active circulators, IEEE Trans. Microw. Theory Techn. **48**, 316 (2000).

[25] S. W. Y. Mung and W. S. Chan, The challenge of active circulators: Design and optimization in future wireless communication, IEEE Microw. Mag. **20**, 55 (2019).

[26] A. Kamal, A parametric device as a nonreciprocal element, Proc. IRE **48**, 1424 (1960).

[27] R. Maurer and K.-H. Locherer, Low-noise nonreciprocal parametric amplifier with power matching at the input and output, Proc. IEEE **51**, 1589 (1963).

[28] J. Hamasaki, A theory of a unilateral parametric amplifier using two diodes, Bell Syst. Tech. J. **43**, 1123 (1964).

[29] A. Kamal, J. Clarke, and M. Devoret, Noiseless nonreciprocity in a parametric active device, Nat. Phys. **7**, 311 (2011).

[30] B. Abdo, K. Sliwa, L. Frunzio, and M. Devoret, Directional amplification with a Josephson circuit, Phys. Rev. X **3**, 031001 (2013).

[31] J. Kerckhoff, K. Lalumière, B. J. Chapman, A. Blais, and K. W. Lehnert, On-Chip Superconducting Microwave Circulator from Synthetic Rotation, Phys. Rev. Appl. **4**, 034002 (2015).

[32] B. J. Chapman, E. I. Rosenthal, J. Kerckhoff, B. A. Moores, L. R. Vale, J. A. B. Mates, G. C. Hilton, K. Lalumière, A. Blais, and K. W. Lehnert, Widely Tunable On-Chip Microwave Circulator for Superconducting Quantum Circuits, Phys. Rev. X **7**, 041043 (2017).

[33] Y. Yu and M. Rinaldi, in *2019 20th International Conference on Solid-State Sensors, Actuators and Microsystems & Eurosensors XXXIII (TRANSDUCERS & EUROSENSORS XXXIII)* (Berlin, Germany, 2019), p. 901.

[34] Z. Xiao, D. L. Sounas, A. Nagulu, M. Tymchenko, T. Dinc, H. Krishnaswamy, and A. Alù, Role of Synchronization in Magnetless Nonreciprocal Devices Based on Commutated Transmission Lines, Phys. Rev. Appl. **13**, 064033 (2020).

[35] D. M. Pozar, *Microwave Engineering* (John wiley & sons, 2011).

[36] Remember that nonreciprocity is a result of signal transmission through sidebands. On the other hand, a direct path between the ports involves no frequency conversion and, thus, it is reciprocal. Therefore, to maximize nonreciprocity, it is important to avoid such a path.

[37] An exception to this case would be if $Z(\omega)$ is a third-order filter, with zeros at $\omega_0' \pm \Omega$ and a pole at ω_0'. However, such a network would be rather complicated in practice and would probably lead to a smaller bandwidth than a single-sideband circuit.